# Selective Mode Conversion and Rainbow Trapping via Graded Elastic Waveguides

Jacopo M. De Ponti,[1,*] Luca Iorio,[1] Emanuele Riva,[2] Raffaele Ardito,[1] Francesco Braghin,[2] and Alberto Corigliano[1]

[1] *Department of Civil and Environmental Engineering, Politecnico di Milano, Piazza Leonardo da Vinci 32, Milano 20133, Italy*

[2] *Department of Mechanical Engineering, Politecnico di Milano, Via Giuseppe La Masa 1, Milano 20156, Italy*

(Received 29 April 2021; revised 3 August 2021; accepted 24 August 2021; published 15 September 2021)

We experimentally achieve wave-mode conversion and rainbow trapping in an elastic waveguide loaded with an array of resonators. Rainbow trapping is a phenomenon that induces wave confinement as a result of a spatial variation of the wave velocity, here promoted by gently varying the length of consecutive resonators. By breaking the geometrical symmetry of the waveguide, we combine the wave-speed reduction with a reflection mechanism that mode converts flexural waves impinging on the array into torsional waves traveling in opposite directions. The framework presented herein may open opportunities in the context of wave manipulation through the realization of structural components with concurrent wave-conversion and energy-trapping capabilities.

DOI: 10.1103/PhysRevApplied.16.034028

## I. INTRODUCTION

The emergence of mechanisms to manipulate the propagation of waves has attracted growing interest across different realms of physics, with multiple realizations in quantum [1], electromagnetic [2,3], acoustic [4–6], and elastic systems [7–17]. In the context of mechanics, a number of works have recently investigated the emergence of nontrivial topological phases in elastic structures, in analogy with relevant forms of behavior previously observed in quantum physics [18]. Notable examples extensively explored in mechanics include defect-immune and scattering-free waveguides, which have been conceived in analogy to the quantum Hall (QH) [19,20], quantum spin Hall (QSH) [21–24], and quantum valley Hall (QVH) effects [25–28]. Other approaches to topology-based design leverage one-dimensional structures augmented by a virtual dimension in parameter space, to access topological properties typically attributed to two-dimensional systems to pursue pumping of elastic waves [29–34] and nonreciprocity [35,36], to name a few. In other words, elastic waveguides are excellent candidates to explore physical phenomena, especially due to the abundance of supported modes with distinct polarizations and coupling among them, which can be relatively simple to establish as compared to the electromagnetic counterparts. While the existence of multiple modes that can hybridize in presence of asymmetry is generally undesired and difficult to grasp, in many cases the break of symmetry creates opportunities by lifting the accidental degeneracies. Mechanical systems with broken symmetries along the thickness direction can be employed for the nucleation of a double-Dirac-cone dispersion that features coupling between otherwise degenerate states, which is the key to emulating the spin-orbital coupling in QSH-based waveguides [24]. Undulated structures have been shown to exhibit frequency gaps and wave directionality due to coupling between axial and flexural vibrations [37,38]. Efficient mode conversion between flexural and longitudinal waves has been achieved through trapped modes with perfect mode conversion (TMPC) in a quasibound state in the continuum (BIC) [39], or the transmodal Fabry-Perot resonance [40]. Other approaches to induce modal coupling leverage nonlinear dynamics, which, however, can often be unpractical due to the large amplitudes required to activate sufficiently strong nonlinear interactions [41,42]. As reported by the aforementioned examples, the additional complexity induced by the symmetry break is often reflected in relevant forms of behavior that are relatively unexplored in the field of mechanics.

A recent line of work employs a graded array of resonators embedded in a host structure to manipulate wave propagation by taking advantage of the resonator-structure interaction. This modulation strategy promotes a wave number transformation that, in turn, activates a spatial decrease of the wave velocity at distinct frequencies, which is the blueprint of the so-called *rainbow effect* [43–47]. Originally discovered in electromagnetic systems in nonuniform linearly tapered planar waveguides

*jacopomaria.deponti@polimi.it

 

with cores of negative-index material [48], the rainbow effect has been pursued within different research fields and through numerous physical platforms, among which are acoustic systems [49–51], water waves [52], and fluid-loaded elastic plates [53]. Similar configurations have been combined with deep elastic substrates to induce conversion between Rayleigh ($R$) and shear ($S$) or pressure ($P$) waves [54–57]. Despite the underlying physics being driven by the spatial variation of the wave speed, the existence of distinct wave modes and the nature of the coupling among them delineate a transition between reflection and trapping mechanisms [58]. The former is induced by resonances and leads to wave scattering at the boundary of the first Brillouin zone. The latter is instead promoted by the coupling between crossing wave modes, typical of the second Brillouin zone, and hereafter employed to achieve concurrent wave-mode conversion and trapping. While the majority of the studies are focused on a single phenomenon, the coexistence of multiple functionalities is not common, especially in the field of mechanics.

Motivated by this and by the opportunity to simultaneously achieve trapping and mode conversion, in this paper we consider an elastic waveguide loaded by a graded array of resonators with variable length. This gradual variation promotes rainbow trapping of flexural waves throughout the array. The considered implementation embodies a broken symmetry with respect to the shear center of the waveguide, which, in turn, activates a mode conversion between impinging flexural waves and torsional waves traveling in the opposite direction through a phenomenon that is known in mechanics as *mode locking* [59]. The numerical and experimental results presented herein demonstrate how a simple structure can be used to confine and mode convert elastic waves, expanding the range of possibilities in the context of wave manipulation and control, with implications of technological relevance for applications involving mechanical vibrations, such as nondestructive evaluation, ultrasonic imaging, and energy harvesting. For instance, flexural and torsional wave modes provide different resolution for nondestructive evaluation and testing, especially due to the associated wavelengths, which allow for the identification of cracks and defects of different shapes and dimensions [60]. Also, different wave-propagation properties (both in terms of wave speed and dispersion) yield different behavior in the context of short- and long-range inspection [61] of mechanical structures [62] and biomedical systems [63–65]. A more straightforward application concerns energy harvesting and enhanced sensing, as extensively discussed in a number of papers [43–47,58].

The paper is organized as follows. In Sec. II, a simplified model for the analysis of symmetry-broken waveguides is presented and employed to tailor a suitable graded profile of locally unbalanced resonators. The theoretical aspects of the trapping and conversion mechanisms are unfolded by way of a dispersion analysis, which is preparatory for the numerical and experimental analysis pursued in Sec. III. Concluding remarks are presented in Sec. IV.

## II. SIMULTANEOUS TRAPPING AND MODE CONVERSION: SIMPLIFIED MODELING AND DESIGN

To elucidate the design paradigm and conditions for selective trapping and reflection, we consider the waveguide displayed in Fig. 1. The implementation consists in a slender beam, which is equipped with a set of attachments of variable length, linearly increasing along the main dimension of the waveguide, to activate the rainbow effect for the asymmetric Lamb $A_0$ (input) wave mode. Each side of the beam accommodates an identical graded array of elements that, in turn, is rigidly connected to the host structure. In addition to the graded profile, the two arrays are spatially shifted by a distance $\xi$, to locally break the geometrical symmetry with respect to the shear center of the cross section. Such a tailored symmetry break drives a spatially growing coupling between transverse motion $w$ and rotation $\phi$ of the waveguide, which are inherently linked to the asymmetric Lamb and torsional $T_0^{-}$ wave modes. This coupling activates a conversion mechanism that can be interpreted in the light of modal interaction between distinct waveguides, according to the schematic in Fig. 1(b). This model represents a conceptual scheme, while the theoretical derivations are obtained from the model in Figs. 1(a) and 1(c), respectively. The schematic illustrates how consecutive resonators locally trigger the transformation between $A_0$ and $T_0$ wave modes, inducing a reflected wave $T_0^{-}$ exiting from the array, as shown in Fig. 1(a), and further wave confinement due to multiple conversion between $T_0 - A_0$ wave modes.

For simplicity, we assume that the further wave modes supported by the waveguide are orthogonal to the excitation mechanism and weakly coupled to the wave modes of relevance, $A_0$ and $T_0$. We also assume that the grading is gentle enough such that the local wave-propagation properties within the array can be deduced from the dispersion curves of the constituent elements. As such, the functional design and conceptual analysis of the grading profile are carried out considering the elastodynamic equations for an Euler-Bernoulli beam dominated by torsional-flexural coupling and loaded with periodic resonators [66]:

$$EI_y w_{,xxxx} + \rho A w_{,tt} = \sum_{r=1}^{2} \sum_{n=-\infty}^{+\infty} m\omega_0^2 \Big[ \Psi_r (x_r + na) + \\ - w (x_r + na) + (-1)^r \frac{b+l}{2} \phi_r (x_r + na) \Big] \delta (x - x_r - na) , \tag{1a}$$

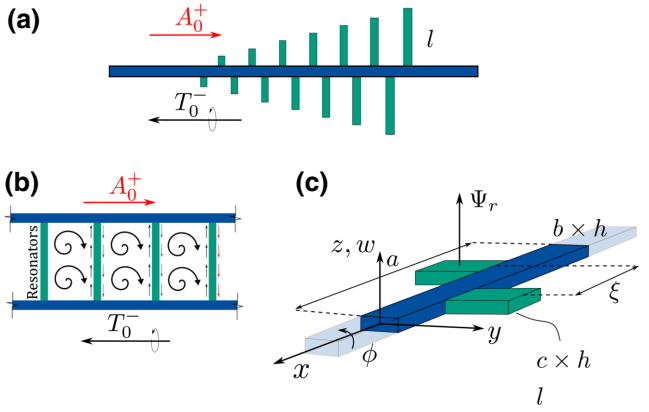


FIG. 1. (a) A graphical representation of the waveguide, which is made of a homogeneous beam rigidly connected to a graded array of resonators that activates the rainbow effect. Due to the broken geometrical symmetry, the waveguide operates as a converter between input $A_0^+$ and output $T_0^-$ wave modes. (b) Idealization of the conversion mechanism: the system can be conceptually interpreted as two distinct elastic waveguides supporting $A_0$ and $T_0$ wave modes, which are coupled using an array of resonators. (c) A schematic of the reference cell, which consists of identical resonator pairs separated by a non-null distance $\xi$, along with the employed reference system.

$$GJ_t\phi_{,xx} - \rho J_p\phi_{,tt} = -\sum_{r=1}^{2}\sum_{n=-\infty}^{+\infty}(-1)^r m\omega_0^2\frac{b+l}{2}$$
$$\left[\Psi_r(x_r+na) + -w(x_r+na)\right.$$
$$\left.+(-1)^r\frac{b+l}{2}\phi_r(x_r+na)\right]\delta(x-x_r-na), \quad (1b)$$

$$\Psi_{r,tt}(x_r+na) + \omega_0^2\left[(-1)^r\frac{b+l}{2}\phi(x_r+na) + \right.$$
$$\left. - w(x_r+na) + \Psi_r(x_r+na)\right] = 0, \quad (1c)$$

where $(\cdot)_{,x}$ denotes the partial derivative $\partial(\cdot)/\partial x$. $w$ and $\phi$ are the vertical displacement and the rotation of the beam, $\Psi_r$ is the displacement of the $n$th resonator in the absolute reference frame. $a = 40$ mm is the lattice size, $EI_y$, $\rho A$, $GJ_t$, and $\rho J_p$ are the elastic and inertial parameters associated with flexural and torsional motion of the beam, consistently with the unit cell and reference frame displayed in Fig. 1(c). $E = 70$ GPa and $\rho = 2710$ kg/m$^3$ are the Young's modulus and the material density; $b = 7$ mm and $h = 2$ mm are the width and thickness of the host waveguide, respectively. For simplicity, the dynamic contribution of the resonator pair is approximated in terms of the equivalent bending stiffness $k$, the participating mass $m$, and the resonance frequency $\omega_0 = \sqrt{\text{k/m}}$, which are dependent upon the resonator geometry $c, l$, and $h$. The Dirac delta function $\delta(x - x_r - na)$ locally accounts for the presence of the resonators, placed at a distance $x_r = a/2 \pm \xi/2$ from the left boundary of the lattice. Additional details on the simplified model are reported in the Supplemental Material [67].

We investigate the dispersion properties $\omega(\mu, l)$ of the waveguide, where $l$ is considered as a free parameter and $\mu = \kappa_x a$ is the normalized wave number. To this end, we consider ansatz solution for the displacement $w(x,t) = \hat{w}(x)\, e^{-j(\kappa_x x - \omega t)}$ and for the rotation $\phi(x,t) = \hat{\phi}(x)\, e^{-j(\kappa_x x - \omega t)}$, where $\hat{w}(x) = \sum_{p=-P}^{P}\hat{w}_p e^{-jn\kappa_m x}$, $\hat{\phi}(x) = \sum_{p=-P}^{P}\hat{\phi}_p e^{-jn\kappa_m x}$ embody the $x$ periodicity of the medium and $\kappa_m = 2\pi/a$ is the modulation wave number. As such, the transverse and torsional motions are approximated in terms of $p = -P, \ldots, +P$ plane-wave components. $P = 3$ is found to be sufficient for an accurate description of the dynamic behavior in the operating-frequency region. Harmonic motion is also assumed for the resonators $\Psi_r(x_r) = \hat{\Psi}_r(x_r)\, e^{j\omega t}$. The application of the plane-wave expansion method (PWEM), the formulation of which is detailed in the Supplemental Material [67], yields the following eigenvalue problem:

$$K(\kappa_x, l)\,\hat{\boldsymbol{\eta}} = \omega^2 M\hat{\boldsymbol{\eta}}, \quad (2)$$

where $K$ and $M$ are the $(2P+2)\times(2P+2)$ stiffness and mass matrices and $\hat{\boldsymbol{\eta}} = \left[\hat{\boldsymbol{w}}, \hat{\boldsymbol{\phi}}, \hat{\Psi}_1, \hat{\Psi}_2\right]^T$ accommodates the vector coefficients for the distinct wave modes and resonator pairs. The solution of the eigenvalue problem $\omega(\kappa_x, l)$ is displayed in Fig. 2(a) for the first three dispersion bands. In the figure, the nature of the motion is discriminated through a color scale proportional to the polarization factor $p = |\int_0^a \hat{w}(x)|^2 / \left(|\int_0^a \hat{w}(x)|^2 + |b\int_0^a \hat{\phi}(x)|^2\right)$, which can be interpreted as a measure of the coupling between waves characterized by distinct polarizations. Thus, a transition from blue to red denotes a transformation from pure rotation to a transverse motion. Some considerations follow. (i) The lone beam features an accidental degeneracy, which corresponds to crossing flexural and rotational dispersion curves when $l \to 0$. As the length of the resonator increases, the geometrical symmetry of the cross section is locally broken and a frequency gap emerges from the otherwise degenerate states; this phenomenon is generally known as *mode locking* in mechanics and is hereafter employed to tailor selective rainbow trapping and reflection. (ii) Interestingly, when the attachment length is smaller than a threshold (i.e., $l \approx 12$ mm), the band-gap formation mechanism is dominated by purely geometrical factors; in contrast, for sufficiently high $l$ values, the resonance frequency of the attachment lies in the

neighborhood of the gap and the nature of the coupling is driven by a combination of broken symmetry and local resonance; in practice, the combination of the two mechanisms yields a flattening of the dispersion curves that is beneficial in terms of wave-velocity decrease and trapping. (iii) In the neighborhood of the gap, the dispersion relation exhibits wave modes characterized by a balanced torsional and flexural motion, especially in relation to the zero-group-velocity region ($a\partial\omega/\partial\mu = 0$); this is of paramount importance for the interplay between wave-conversion and energy-trapping mechanisms, which will be discussed in the remainder of this section.

The functional design of the graded profile of resonators is accomplished following the general guidelines provided in prior works [43,45]. That is, rainbow trapping is hereafter pursued targeting a group-velocity decrease along the beam at an operating frequency $f = 2.12$ kHz. To that end, $l$ is denoted as the relevant parameter linearly varied along the main dimension of the beam. Such a variation yields a local wave number distribution $\mu(l)$ highlighted with black dots in Fig. 2(a) The colored version of the isofrequency line $\mu(l)$ is reported in Fig. 2(b), illustrating that a variation of $l$ not only activates wave modes characterized by different wave numbers $\mu$ but also

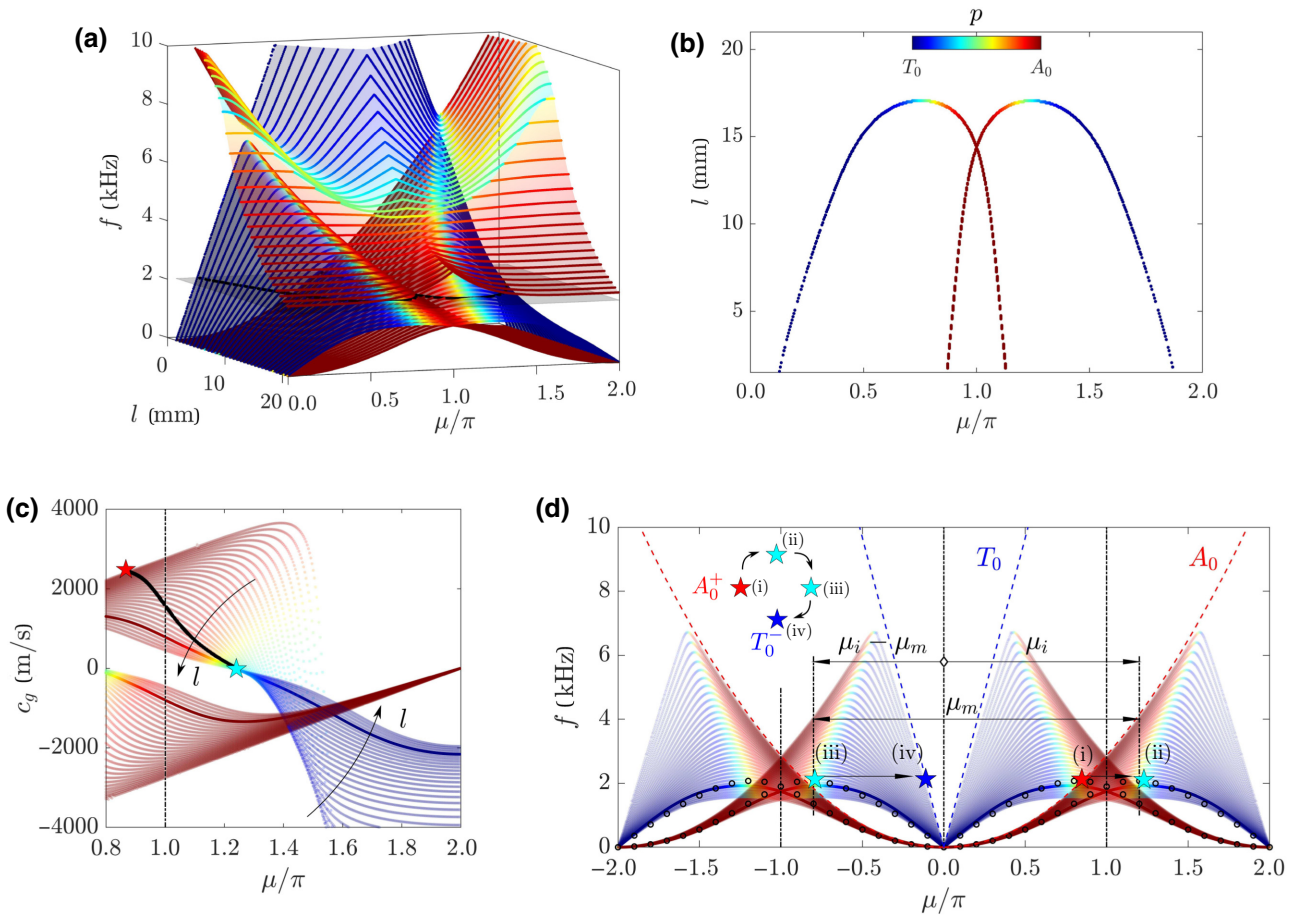


FIG. 2. (a) The dispersion surface $\omega(\mu, l)/2\pi$. For ease of visualization, only the first three dispersion surfaces are displayed. The color is proportional to the polarization factor $p$, which allows us to discriminate between rotation $\phi$ and vertical displacement. Due to the broken symmetry and local resonance, the second and third dispersion surfaces are separated by a frequency gap. The isofrequency line, highlighted in black, represents the operating frequency of the structure, while the colored version is reported in (b). (c) The group velocity $c_g$ upon varying the length of the resonators $l$ with change step $\Delta l = 0.315$ mm, for the first two dispersion bands. In the figure, the group-velocity line associated with the target dispersion branch is highlighted with darker dots. Such a target branch corresponds to the dispersion tangent to the isofrequency line displayed in (b). The group velocity $c_g(l)$ computed for the target frequency is superimposed on the colored plot with black dots. (d) The dispersion relation $\omega(\mu)$ upon varying $l$. (d) The schematic representation with coloured stars illustrates the conversion mechanism that takes place in correspondance of the target resonator. The system is excited through the $A_0^+$ wave mode, shown by the red star (i), which is wave number transformed to the cyan star (ii), due to the grading. As the wave reaches the zero-group-velocity region within the second Brillouin zone, it is backscattered to the cyan star (iii) by a quantity equal to the reciprocal lattice vector $\mu_m$ and wave number transformed to the back-traveling $T_0^-$ wave mode marked with the blue star (iv). The black dots represent the numerical solution computed in COMSOL Multiphysics.

promotes a transformation between distinct polarizations (colored dots). Consistently, the colored group-velocity profile $c_g\,[\omega(\mu), l] = a\partial\omega/\partial\mu$, is evaluated by finite difference for the entire wave number parameter space and represented in Fig. 2(c) for the first two dispersion branches. For ease of visualization, the second dimension $l$ is eliminated and substituted with arrows, to better illustrate the group-velocity profile $c_g\,[\omega(\mu)]$ in response to a variation of $l$. Here, the target dispersion curve, i.e., the dispersion branch that touches the isofrequency line with zero group velocity, is represented with darker-colored dots. As the length of the resonator $l$ is modified in space, the dispersion properties at the operating frequency naturally follow the black curve $\mu\,(l)$ displayed in Fig. 2(a). This modification is accompanied by a change in the group velocity $c_g\,(l)$ highlighted with black dots in Fig. 2(c) and, in turn, terminates in the zero-group-velocity region away from the edges of the Brillouin zone, which is the key factor in achieving rainbow trapping [58]. The analysis shows that the wave-speed transformation is accompanied by a change in the polarization from a purely flexural mode that terminates in a region in which the wave is characterized by a mixed torsional-flexural motion and $c_g \approx 0$.

In addition to the rainbow effect, the tailored broken symmetry of the array is responsible for a reflection mechanism that mode converts the impinging flexural waves into torsional waves traveling in the opposite direction. This mechanism is discussed hereafter assuming that most of the conversion takes place in relation to the zero-group-velocity region, where the coupling is maximum. As such, among the possible dispersion branches, we focus on the (target) curve highlighted with darker-colored dots in Figs. 2(c) and 2(d) and we assume that a smooth variation of $l$ is provided to reach the target curve. Now, consider an input wave $A_0^+$, represented in Fig. 2(d) by the red star (*i*). Such a wave impinges on the graded array of resonators and, due to the smooth variation of $l$ in space, the wave mode experiences a wave number transformation that drives the transfer of spectral content to the cyan star (*ii*), where the group velocity at the operating frequency is ideally nullified and the normalized wave number is $\mu = \mu_i$. It is worth mentioning that the group velocity can reach a zero value only for infinitely long arrays, while for a finite number of elements the wave propagation occurs with decreased speed and, therefore, the positive-going component impinges on the following resonators. Due to the conservation of the crystal momentum, the traveling wave is backscattered to $\mu = \mu_i - \mu_m$ and, once again, is wave number transformed from the cyan star (*iii*) to the blue star (*iv*) as a result of the linear decrease of $l$, which produces a back-propagating torsional wave mode $T_0^-$ exiting the graded array. Due to the limited number of resonators, a small amount of energy does not follow this path, leading to a backscattered flexural wave $A_0^-$ with spectral content $\mu = -\mu_i$, which is delayed in time consistently with the wave-speed reduction described by the dispersion analysis. In accordance with the above arguments and provided that only a small amount of energy does not follow such a wave number transformation in the back-propagating path, the conversion efficiency of such a system is close to 100%. A more detailed discussion on this matter is provided in the Supplemental Material [67].

To conclude the design of the graded array, the numerical dispersion relation is evaluated numerically via the COMSOL Multiphysics environment spanning the parameter space $l \in [0, 22]$ mm and reported with black circles in Fig. 2(d) for the target dispersion curve. According to the analysis, the necessary array of resonators to reach near-zero group velocity is characterized by initial and final (target) lengths of $l_1 = 8$ mm and $l_7 = 18.3$ mm, respectively, which are distributed along $L = 7a$ mm for a number of $N = 7$ cells. The array is then continued to a final length of $l_9 = 21.2$ mm to prevent wave propagation through the array for frequencies in the neighborhood of the target mode.

## III. THEORY MEETS EXPERIMENTS

The discussion is now focused on the transient analysis of wave propagation simulated in the ABAQUS implicit environment [68], to corroborate the theoretical claims. The implementation consists in a homogeneous beam that serves as input domain for right-traveling waves, which is followed by the graded array of resonators. Undesired reflections are avoided by way of absorbing boundaries applied to the left and right ends of the beam [69]. A transverse force with central frequency $f_0 = 2.12$ kHz, width $\Delta f = 0.14$ kHz, and a time duration of 15 ms is employed to provide excitation and to confine the energy content in the neighborhood of the operating frequency. Additional details on the numerical methods are reported in the Supplemental Material [67].

Numerical results for consecutive time instants $t_0 = 2, 6, 10, 12$ ms are displayed in Fig. 3(a). As expected, at the beginning of the time simulation, the motion is dominated by flexural waves. As time elapses, part of the energy is transferred to torsional wave modes, starting from the snapshot captured in Fig. 3(a)II at $t_0 = 6$ ms, where the homogeneous trait is dominated by transverse waves and the graded array exhibits rotation, due to the broken geometrical symmetry. In contrast, the displacement field displayed in Fig. 3(a)III–IV is characterized by mixed wave motion within the entire spatial domain. These considerations are further confirmed by the numerical dispersion $\hat{d}\left(\kappa_x, \kappa_y, \omega\right) = \sqrt{\hat{w}^2 + \hat{u}^2 + \hat{v}^2}$, which is illustrated alongside the displacement fields in Fig. 3(a), where $\hat{w} = \hat{w}\left(\kappa_x, \kappa_y, \omega\right)$, $\hat{v} = \hat{w}\left(\kappa_x, \kappa_y, \omega\right)$, and $\hat{u} = \hat{w}\left(\kappa_x, \kappa_y, \omega\right)$ are the three-dimensional (3D) Fourier-transformed displacement fields of the homogeneous part of the waveguide. To evaluate the numerical dispersion, the time histories

$w(x,y,t)$, $v(x,y,t)$, and $u(x,y,t)$ are windowed in the neighborhood of the probed time instants $t_0$ by way of a suitable Gaussian function $g(t) = e^{-(t-t_0)^2/2c^2}$, where $c$ is a parameter that controls the width of the Gaussian function. For ease of visualization, the numerical dispersion is reduced to $\hat{d}(\kappa_x, \omega)$ by taking the root-mean-square (rms) value along $\kappa_y$, which yields the diagram displayed in the figure. As expected, the spectral content in the waveguide is initially located in the positive half of the reciprocal space and relates to the $A_0^+$ dispersion branch. When the flexural wave reaches the array, the wave is trapped and converted into a component traveling in the opposite direction, corresponding to the $T_0^-$ and the $A_0^-$ dispersion branches exiting the graded array. The concept is elucidated in the spectrogram displayed in Fig. 3(b), which is obtained by smoothly varying the position of the

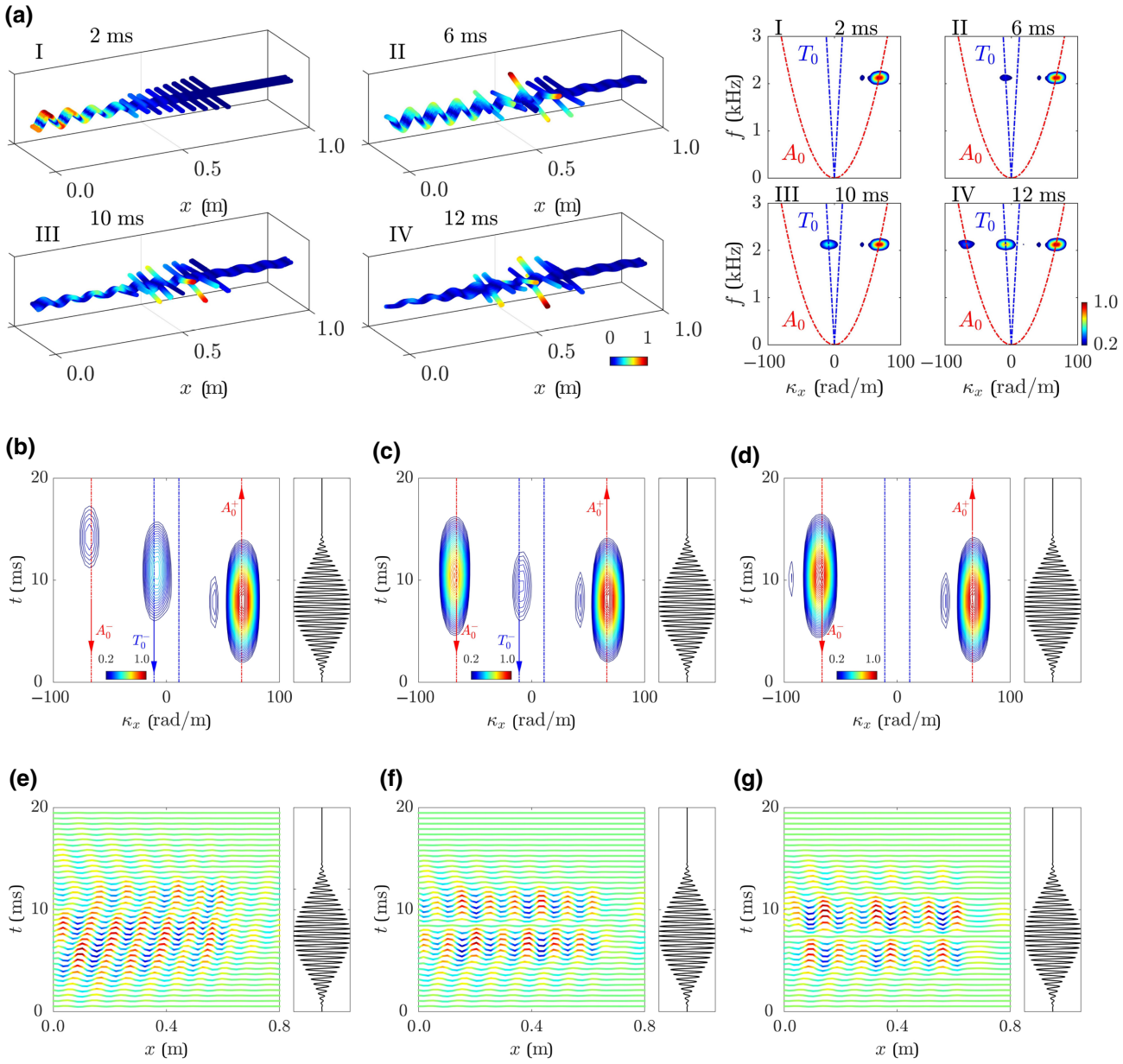


FIG. 3. (a) The numerical displacement field measured at different time instants for an input wave mode $A_0^+$, along with the corresponding dispersion relations for a waveguide endowed with absorbing boundaries. The diagrams show that the input wave is reflected and converted from $A_0^+$ to $T_0^-$ in time. (b)–(d) The spectrograms display the temporal evolution of the spectral content for (b) a waveguide with the graded array of resonators; (c) a waveguide without the initial part of the grading, i.e., with only resonators 7–9; and (d) a homogeneous waveguide, without the array of resonators. The excitation signal is shown alongside the spectrogram. The input wave is confined, trapped, and delayed only if the complete array of resonators is present. (e)–(g) The corresponding out-of-plane displacement field filtered to separate the contribution of the $A_0$ wave mode.

Gaussian function spanning the range $t_0 \in [0, 20]$ ms. Also, the dependence on the frequency is eliminated by taking the rms value, which results in the amplitude $\hat{d}(\kappa_x, t_0)$. The same analysis is performed on a beam without the initial part of the array [see Fig. 3(c)], responsible for the wave-speed reduction, and on a homogeneous beam without a graded array of resonators [reported in Fig. 3(d)] but equipped with clamps corresponding to resonators $N = 8, 9$.

A qualitative comparison of Figs. 3(b)–3(d) reveals that: (i) the presence of the graded array shifts the backward-propagating wave $A_0^-$ by 5 ms, as a result of the tailored trapping mechanism, while the backward-propagating $A_0^-$ component is not delayed in a relevant way in the event that the initial part of the array is not considered; (ii) the wave-speed reduction is accompanied by a transfer of energy between the $A_0^+$ and $T_0^-$ wave modes, which occurs approximately 3 ms before the $A_0^-$ wave mode back propagates; (iii) the amount of conversion is dramatically reduced in the event that the first part of the array is not present. To further confirm that the graded array operates as a delay line and mode converter for flexural and/or torsional waves, the displacement field $w(x, y, t)$ is filtered in the wave number domain for $\kappa_x$ values outside 40 rad/m and 100 rad/m. The filtered displacement field allows us to isolate and graphically visualize the $A_0$ mode evolution in time, which is displayed in Figs. 3(e)–3(g) for the three reference configurations. As expected, only if the graded array is present, the numerical wave field is altered in such a way that the energy slowly vanishes and is mode converted to the counterpropagating $T_0^-$ wave mode. It is also worth noting that the conversion efficiency is very high, as most of the energy, initially injected into $A_0^+$, is converted into the $T_0^-$ back-propagating mode. The nonconverted energy is instead back-reflected as a $A_0^-$ mode and shifted in time, consistently with the above discussion. Additional analyses on the conversion efficiency are performed on structures with longer input domains and with variation of the number of pair resonators (9, 25, and 50). Such analyses are reported and discussed in the Supplemental Material [67] and demonstrate that for a sufficiently long system compliant with the theoretical arguments, the conversion efficiency is close to 100%.

The numerical results are validated through an experimental analysis in the transient regime, which is performed on a structure identical to the one employed in the simulations, except for the boundary conditions that are discussed hereafter. The schematic of the experimental setup is shown in Fig. 4. The system is rigidly connected to a LDS v406 electrodynamic shaker, to provide excitation, while the opposite end is clamped to ground, to avoid excessive geometrical deformation. The wave field is measured on the surface of the system through a Polytec 3D scanner laser doppler vibrometer (SLDV), which is able to separate the 3D velocity field in both space and time. The

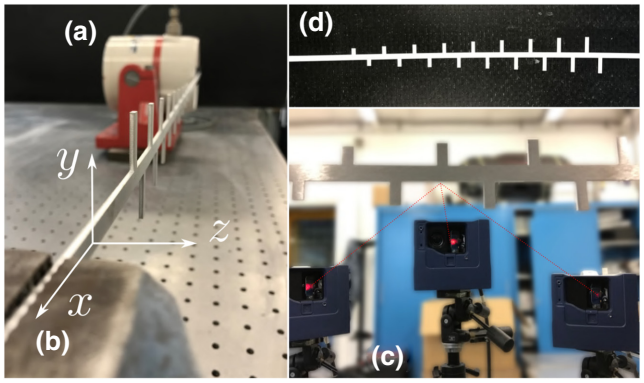


FIG. 4. The experimental setup employed to measure wave propagation. The waveguide is excited using an electrodynamic shaker (a), while the opposite side is clamped (b). Wave propagation is measured on the surface of the waveguide through a Polytec 3D scanner laser doppler vibrometer (c), which is able to separate the 3D velocity field. The top view of the graded array is also provided (d).

excitation signal is synchronously started with the acquisition, which, in turn, is averaged in time to decrease the noise. Additional information on the experimental methods is reported in the Supplemental Material [67]. The experimental results in terms of the 3D displacement field $w(x, y, t)$, $v(x, y, t)$, and $u(x, y, t)$, along with the corresponding dispersion $\hat{d}(\kappa_x, \omega)$ centered at different time instants, $t_0$ are displayed in Fig. 5(a) and are similar to those displayed in Fig. 3(a). After the input $A_0^+$ mode is injected into the structure, part of the energy is mode converted in a torsional $T_0^\pm$ mode and part is delayed in time. In contrast to the results displayed in Fig. 3(a), the propagating waves cannot escape the system and the amount of dissipation is negligible. We also observe that, in comparison to the numerical case study, the mode conversion takes place in a shorter time and the associated amplitude is greater. This is attributed to: (i) the absence of absorbing boundaries, which facilitates the accumulation of energy, especially that transferred to the torsional wave mode characterized by a faster propagation speed, and triggers the formation of a standing mode; and (ii) the presence of misalignment and imperfections that facilitate the conversion between wave modes that populate the dispersion at the operating frequency.

The same considerations apply for the experimental and numerical spectrograms in Figs. 5(b) and 5(c). The figures illustrate a similar amount of delay between incident $A_0^+$ and reflected $A_0^-, T_0^-$ wave modes, whereas in the experimental diagram in Fig. 5(b) we observe an extra conversion amplitude between the $A_0$ and $T_0$ waves that is triggered by the undesired curvature of the beam, due to the manufacturing process, which is not present in the numerical analysis. Also, consistently with the simulation performed with absorbing boundaries [Fig. 3(b)], the converted $A_0^-$

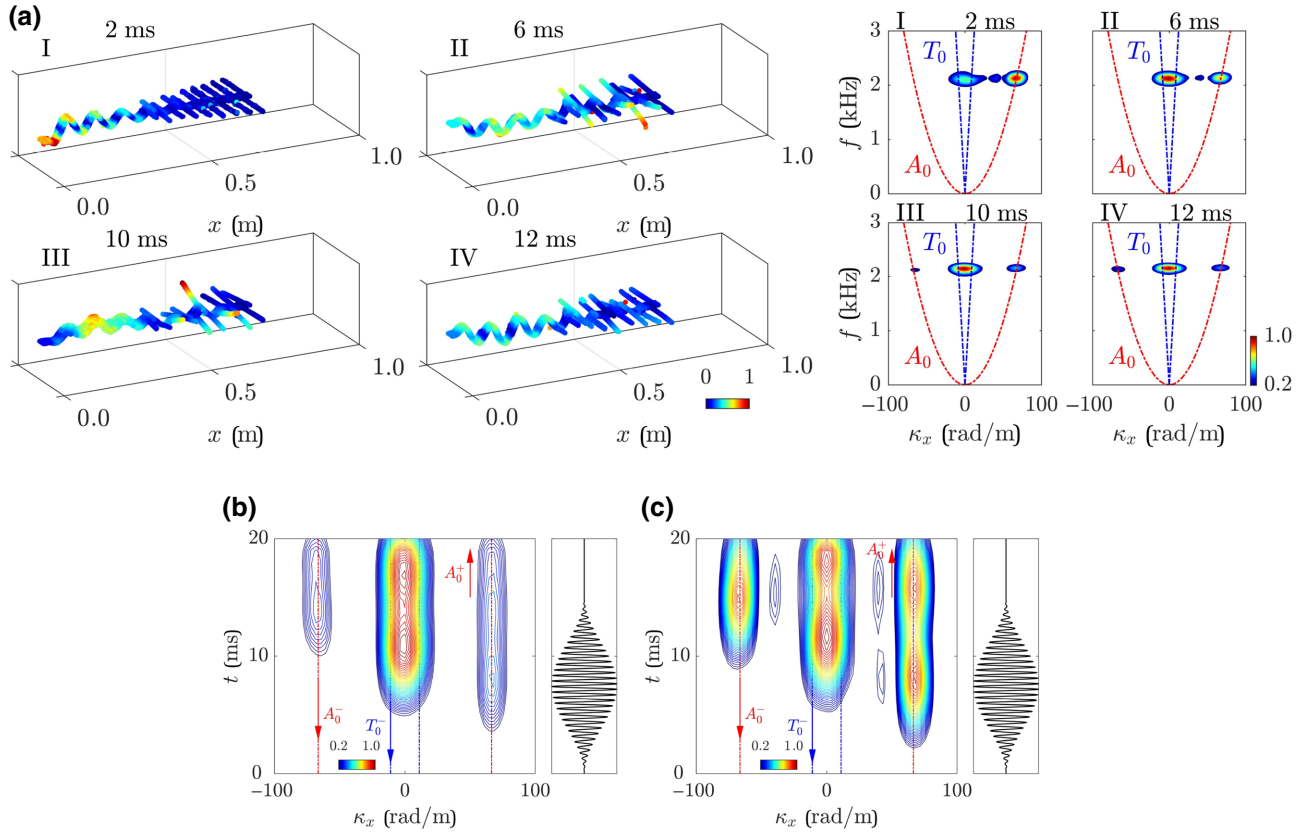


FIG. 5. (a) The experimental velocity field and the corresponding dispersion relation measured at different time instants. The (b) experimental and (c) numerical spectrograms, illustrating the evolution of the spectral content in time. The experimental and numerical results are characterized by a comparable temporal delay for the $A_0^-$ wave mode, while different conversion amplitudes are observed, due to the presence of imperfections and misalignments that enhance the torsional coupling.

wave mode is delayed by the same amount as for the experimental data displayed in Fig. 5(b), which further confirms that the rainbow trapping occurs as expected. We finally note that an additional $T_0^+$ component is measured; this is attributed to the finite length of the system, which allows for spurious edge reflections of the $T_0^-$ waves exiting the array.

## IV. CONCLUSIONS

In this paper, we experimentally realize a graded structure that is capable of converting flexural waves into torsional waves traveling in the opposite direction. Such a conversion is accompanied by trapping of flexural waves that are delayed while propagating through the array. The complex interplay between trapping and conversion is explained in terms of dispersion analysis, where the dynamic behavior is dominated by a local symmetry break and the smooth variation of the resonator length in space, which locally activates the energy transfer between distinct wave modes and globally determines a wave-speed reduction. The concept can be generalized to multidimensional or multiphysics systems characterized by a coupling induced between waves of a different nature, such as in piezophononic structures [70,71], in microelectromechanical systems, or through fluid-structure interactions [53]. This may open opportunities in the context of wave manipulation and control in metamaterial structures with concurrent wave-conversion and energy-trapping capabilities. Concerning future developments in this direction, our implementation can be easily scaled and adapted to operate at the microscale, to pursue energy harvesting and wave conversion.

## ACKNOWLEDGMENTS

The support of the H2020 FET-proactive Metamaterial Enabled Vibration Energy Harvesting (MetaVEH) project under Grant Agreement No. 952039 is acknowledged. We also gratefully acknowledge the Italian Ministry of Education, University, and Research for the support provided through the Project "Department of Excellence LIS4.0—Lightweight and Smart Structures for Industry 4.0."

[1] H. M. Zahid and C. L. Kane, Colloquium: Topological insulators, Rev. Mod. Phys. **82**, 3045-3067 (2010).

[2] L. Ling, J. D. Joannopoulos, and M. Soljačić, Topological photonics, Nat. Photonics **8**, 821 (2014).

[3] A. B. Khanikaev, S. H. Mousavi, W.-K. Tse, M. Kargarian, A. H. MacDonald, and G. Shvets, Photonic topological insulators, Nat. Mater. **12**, 233 (2013).

[4] S. A. Cummer, J. Christensen, and A. Alù, Controlling sound with acoustic metamaterials, Nat. Rev. Mater. **1**, 16001 (2016).

[5] G. Ma and P. Sheng, Acoustic metamaterials: From local resonances to broad horizons, Sci. Adv. **2**, e1501595 (2016).

[6] Z. Yang, F. Gao, X. Shi, X. Lin, Z. Gao, Y. Chong, and B. Zhang, Topological Acoustics, Phys. Rev. Lett. **114**, 114301 (2015).

[7] H. Nassar, B. Yousefzadeh, R. Fleury, M. Ruzzene, A. Alù, C. Daraio, A. N. Norris, G. Huang, and M. R. Haberman, Nonreciprocity in acoustic and elastic materials, Nat. Rev. Mater. **5**, 667 (2020).

[8] Y. F. Wang, Y. Z. Wang, B. Wu, W. Chen, and Y. S. Wang, Tunable and active phononic crystals and metamaterials, Appl. Mech. Rev. **72**, 040801 (2020).

[9] M. I. Hussein, M. J. Leamy, and M. Ruzzene, Dynamics of phononic materials and structures: Historical origins, recent progress, and future outlook, Appl. Mech. Rev. **66**, 040802 (2014).

[10] C. Sugino and A. Erturk, Analysis of multifunctional piezoelectric metastructures for low-frequency bandgap formation and energy harvesting, J. Phys. D: Appl. Phys. **51**, 215103 (2018).

[11] E. G. Williams, P. Roux, M. Rupin, and W. A. Kuperman, Theory of multiresonant metamaterials for $A_0$ Lamb waves, Phys. Rev. B **91**, 104307 (2015).

[12] C. Sugino, S. Leadenham, M. Ruzzene, and A. Erturk, On the mechanism of bandgap formation in locally resonant finite elastic metamaterials, J. Appl. Phys. **120**, 134501 (2016).

[13] S. D. M. Adams, R. V. Craster, and S. Guenneau, Guided and standing Bloch waves in periodic elastic strips, Waves Random Complex Media **19**, 321 (2009).

[14] V. Pagneux and A. Maurel, Lamb wave propagation in inhomogeneous elastic waveguides, Proc. R. Soc. A **462**, 1315 (2006).

[15] A. Khelif, B. Djafari-Rouhani, J. O. Vasseur, and P. A. Deymier, Transmission and dispersion relations of perfect and defect-containing waveguide structures in phononic band gap materials, Phys. Rev. B **68**, 024302 (2003).

[16] Y. Pennec, B. D. Rouhani, C. Li, J. M. Escalante, A. Martinez, S. Benchabane, V. Laude, and N. Papanikolaou, Band gaps and cavity modes in dual phononic and photonic strip waveguides, AIP Adv. **1**, 041901 (2011).

[17] R. V. Craster, S. Guenneau, and S. D. M. Adams, Mechanism for slow waves near cutoff frequencies in periodic waveguides, Phys. Rev. B **79**, 045129 (2009).

[18] S. D. Huber, Topological mechanics, Nat. Phys. **12**, 621 (2016).

[19] P. Wang, L. Lu, and K. Bertoldi, Topological Phononic Crystals with One-Way Elastic Edge Waves, Phys. Rev. Lett. **115**, 104302 (2015).

[20] H. Chen, L. Y. Yao, H. Nassar, and G. L. Huang, Mechanical Quantum Hall Effect in Time-Modulated Elastic Materials, Phys. Rev. Appl. **11**, 044029 (2019).

[21] R. Süsstrunk and S. D. Huber, Observation of phononic helical edge states in a mechanical topological insulator, Science **349**, 47 (2015).

[22] H. Chen, H. Nassar, A. N. Norris, G. K. Hu, and G. L. Huang, Elastic quantum spin Hall effect in kagome lattices, Phys. Rev. B **98**, 094302 (2018).

[23] R. Chaunsali, C. W. Chen, and J. Yang, Subwavelength and directional control of flexural waves in zone-folding induced topological plates, Phys. Rev. B **97**, 054307 (2018).

[24] M. Miniaci, R. K. Pal, B. Morvan, and M. Ruzzene, Experimental Observation of Topologically Protected Helical Edge Modes in Patterned Elastic Plates, Phys. Rev. X **8**, 031074 (2018).

[25] E. Riva, D. E. Quadrelli, G. Cazzulani, and F. Braghin, Tunable in-plane topologically protected edge waves in continuum kagome lattices, J. Appl. Phys. **124**, 164903 (2018).

[26] J. Vila, R. K. Pal, and M. Ruzzene, Observation of topological valley modes in an elastic hexagonal lattice, Phys. Rev. B **96**, 134307 (2017).

[27] T. W. Liu and F. Semperlotti, Tunable Acoustic Valley-Hall Edge States in Reconfigurable Phononic Elastic Waveguides, Phys. Rev. Appl. **9**, 014001 (2018).

[28] T. W. Liu and F. Semperlotti, Experimental Evidence of Robust Acoustic Valley Hall Edge States in a Nonresonant Topological Elastic Waveguide, Phys. Rev. Appl. **11**, 014040 (2019).

[29] M. I. Rosa, R. K. Pal, J. R. Arruda, and M. Ruzzene, Edge States and Topological Pumping in Spatially Modulated Elastic Lattices, Phys. Rev. Lett. **123**, 034301 (2019).

[30] Y. Xia, A. Erturk, and M. Ruzzene, Topological Edge States in Quasiperiodic Locally Resonant Metastructures, Phys. Rev. Appl. **13**, 014023 (2020).

[31] E. Riva, M. I. Rosa, and M. Ruzzene, Edge states and topological pumping in stiffness-modulated elastic plates, Phys. Rev. B **101**, 094307 (2020).

[32] I. H. Grinberg, M. Lin, C. Harris, W. A. Benalcazar, C. W. Peterson, T. L. Hughes, and G. Bahl, Robust temporal pumping in a magneto-mechanical topological insulator, Nat. Commun. **11**, 974 (2020).

[33] E. Riva, V. Casieri, F. Resta, and F. Braghin, Adiabatic pumping via avoided crossings in stiffness-modulated quasiperiodic beams, Phys. Rev. B **102**, 014305 (2020).

[34] W. Cheng, E. Prodan, and C. Prodan, Experimental Demonstration of Dynamic Topological Pumping across Incommensurate Bilayered Acoustic Metamaterials, Phys. Rev. Lett. **125**, 224301 (2020).

[35] J. Marconi, E. Riva, M. Di Ronco, G. Cazzulani, F. Braghin, and M. Ruzzene, Experimental Observation of Nonreciprocal Band Gaps in a Space-Time-Modulated Beam Using a Shunted Piezoelectric Array, Phys. Rev. Appl. **13**, 031001 (2020).

[36] M. A. Attarzadeh, J. Callanan, and M. Nouh, Experimental Observation of Nonreciprocal Waves in a Resonant Metamaterial Beam, Phys. Rev. Appl. **13**, 021001 (2020).

[37] G. Trainiti, J. J. Rimoli, and M. Ruzzene, Wave propagation in periodically undulated beams and plates, Int. J. Solids. Struct. **75-76**, 260 (2015).

[38] G. Trainiti, J. J. Rimoli, and M. Ruzzene, Wave propagation in undulated structural lattices, Int. J. Solids. Struct. **97–98**, 431 (2016).

[39] L. Cao, Y. Zhu, Y. Xu, S. W. Fan, Z. Yang, and B. Assouar, Elastic bound state in the continuum with perfect mode conversion, J. Mech. Phys. Solids **154**, 104502 (2021).
[40] J. M. Kweun, H. J. Lee, J. H. Oh, H. M. Seung, and Y. Y. Kim, Transmodal Fabry-Pérot Resonance: Theory and Realization with Elastic Metamaterials, Phys. Rev. Lett. **118**, 205901 (2017).
[41] W. Jiao and S. Gonella, Intermodal and Subwavelength Energy Trapping in Nonlinear Metamaterial Waveguides, Phys. Rev. Appl. **10**, 024006 (2018).
[42] R. Ganesh and S. Gonella, From Modal Mixing to Tunable Functional Switches in Nonlinear Phononic Crystals, Phys. Rev. Lett. **114**, 054302 (2015).
[43] J. M. De Ponti, A. Colombi, R. Ardito, F. Braghin, A. Corigliano, and R. V. Craster, Graded elastic metasurface for enhanced energy harvesting, New J. Phys. **22**, 013013 (2019).
[44] J. M. De Ponti, A. Colombi, E. Riva, R. Ardito, F. Braghin, A. Corigliano, and R. V. Craster, Experimental investigation of amplification, via a mechanical delay-line, in a rainbow-based metamaterial for energy harvesting, Appl. Phys. Lett. **117**, 143902 (2020).
[45] J. M. De Ponti, *Graded Elastic Metamaterials for Energy Harvesting* (Springer International Publishing, Switzerland, 2021), ISBN 978-3-030-69059-5.
[46] M. Alshaqaq and A. Erturk, Graded multifunctional piezoelectric metastructures for wideband vibration attenuation and energy harvesting, Smart Mater. Struct. **30**, 015029 (2021).
[47] G. J. Chaplain, J. M. De Ponti, G. Aguzzi, A. Colombi, and R. V. Craster, Topological Rainbow Trapping for Elastic Energy Harvesting in Graded Su-Schrieffer-Heeger Systems, Phys. Rev. Appl. **14**, 054035 (2020).
[48] K. L. Tsakmakidis, A. D. Boardman, and O. Hess, 'Trapped rainbow' storage of light in metamaterials, Nature **450**, 397 (2007).
[49] J. Zhu, Y. Chen, X. Zhu, F. J. Garcia-Vidal, X. Yin, W. Zhang, and X. Zhang, Acoustic rainbow trapping, Sci. Rep. **3**, 1728 (2013).
[50] V. Romero-García, R. Picó, A. Cebrecos, V. J. Sánchez-Morcillo, and K. Staliunas, Enhancement of sound in chirped sonic crystals, Appl. Phys. Lett. **102**, 091906 (2013).
[51] A. Cebrecos, R. Picó, V. J. Sánchez-Morcillo, K. Staliunas, V. Romero-García, and L. M. Garcia-Raffi, Enhancement of sound by soft reflections in exponentially chirped crystals, AIP Adv. **4**, 124402 (2014).
[52] L. G. Bennetts, M. A. Peter, and R. V. Craster, Graded resonator arrays for spatial frequency separation and amplification of water waves, J. Fluid Mech. **854**, R4 (2018).
[53] E. A. Skelton, R. V. Craster, A. Colombi, and D. J. Colquitt, The multi-physics metawedge: Graded arrays on fluid-loaded elastic plates and the mechanical analogues of rainbow trapping and mode conversion, New J. Phys. **20**, 053017 (2018).
[54] A. Colombi, D. Colquitt, P. Roux, S. Guenneau, and R. V. Craster, A seismic metamaterial: The resonant metawedge, Sci. Rep. **6**, 1 (2016).
[55] A. Colombi, V. Ageeva, R. J. Smith, A. Clare, R. Patel, M. Clark, D. Colquitt, P. Roux, S. Guenneau, and R. V. Craster, Enhanced sensing and conversion of ultrasonic Rayleigh waves by elastic metasurfaces, Sci. Rep. **7**, 6750 (2017).
[56] D. Colquitt, A. Colombi, R. Craster, P. Roux, and S. Guenneau, Seismic metasurfaces: Sub-wavelength resonators and rayleigh wave interaction, J. Mech. Phys. Solids **99**, 379 (2017).
[57] G. J. Chaplain, J. M. De Ponti, A. Colombi, R. Fuentes-Dominguez, P. Dryburg, D. Pieris, R. J. Smith, A. Clare, M. Clark, and R. V. Craster, Tailored elastic surface to body wave Umklapp conversion, Nat. Commun. **11**, 1 (2020).
[58] G. J. Chaplain, D. Pajer, J. M. De Ponti, and R. V. Craster, Delineating rainbow reflection and trapping with applications for energy harvesting, New J. Phys. **22**, 063024 (2020).
[59] B. R. Mace and E. Manconi, Wave motion and dispersion phenomena: Veering, locking and strong coupling effects, J. Acoustical Soc. Am. **131**, 1015 (2012).
[60] D. E. Chimenti, Guided waves in plates and their use in materials characterization, Appl. Mech. Rev. **50**, 247 (1997).
[61] P. Wilcox, M. Lowe, and P. Cawley, The effect of dispersion on long-range inspection using ultrasonic guided waves, NDT E Int. **34**, 1 (2001).
[62] D. A. Ramatlo, C. S. Long, P. W. Loveday, and D. N. Wilke, A modelling framework for simulation of ultrasonic guided wave-based inspection of welded rail tracks, Ultrasonics **108**, 106215 (2020).
[63] G. T. Clement, P. J. White, and K. Hynynen, Enhanced ultrasound transmission through the human skull using shear mode conversion, J. Acoust. Soc. Am. **115**, 1356 (2004).
[64] P. White, G. Clement, and K. Hynynen, Longitudinal and shear mode ultrasound propagation in human skull bone, Ultrasound Med. Biol. **32**, 1085 (2006).
[65] K. Hynynen, N. McDannold, N. A. Sheikov, F. A. Jolesz, and N. Vykhodtseva, Local and reversible blood-brain barrier disruption by noninvasive focused ultrasound at frequencies suitable for trans-skull sonications, NeuroImage **24**, 12 (2005).
[66] J. Achenbach, *Wave Propagation in Elastic Solids* (Elsevier, New York, 2012), Vol. 16.
[67] See the Supplemental Material at http://link.aps.org/supplemental/10.1103/PhysRevApplied.16.034028 for more details on the simulation procedures, experimental setup, and methodology.
[68] H. M. Hilber, T. J. R. Hughes, and R. L. Taylor, Improved numerical dissipation for time integration algorithms in structural dynamics, Earthquake Eng. Struct. Dyn. **5**, 283 (1977).
[69] P. Rajagopal, M. Drozdz, E. A. Skelton, M. J. Lowe, and R. V. Craster, On the use of absorbing layers to simulate the propagation of elastic waves in unbounded isotropic media using commercially available finite element packages, NDT E Int. **51**, 30 (2012).
[70] A. E. Bergamini, M. Zündel, E. A. Flores Parra, T. Delpero, M. Ruzzene, and P. Ermanni, Hybrid dispersive media with controllable wave propagation: A new take on smart materials, J. Appl. Phys. **118**, 154310 (2015).
[71] S. Alan, A. Allam, and A. Erturk, Programmable mode conversion and bandgap formation for surface acoustic waves using piezoelectric metamaterials, Appl. Phys. Lett. **115**, 093502 (2019).